XCal: A Model-Based Approach to X-ray CT Spectral Calibration

WENRUI LI,[1,*] K. ADITYA MOHAN,[2] VENKATESH SRIDHAR,[2] XIN LIU,[2] JEAN-BAPTISTE FORIEN,[2] JOSEPH BENDAHAN,[2] SARANSH SINGH,[2] GREGERY T. BUZZARD,[1] AND CHARLES A. BOUMAN[1]

[1]*Purdue University, West Lafayette, IN 47907, USA*
[2]*Lawrence Livermore National Laboratory, Livermore, CA 94550, USA*
[*]*liwr5damon@gmail.com*

Abstract: Transmission X-ray computed tomography (CT) is widely used to quantitatively reconstruct 3D objects composed of multiple materials. However, accurate CT reconstruction requires the system to be calibrated to account for the effective X-ray spectrum. Unfortunately, measurement of the effective spectrum is ill-posed, and existing calibration methods require that the system be recalibrated when the system parameters are changed.

In this paper, we propose XCal, a multi-energy model-based spectral calibration approach for X-ray CT. The XCal approach models the effective spectrum using a separable physics-based model of the CT system. The model parameters are then estimated by fitting calibration data with known objects at multiple energies. An important advantage of XCal is that it allows the user to change scanner settings, such as the source voltage or X-ray filters, without the need for recalibration. Evaluations on simulated and measured datasets demonstrate that XCal significantly improves the accuracy of the estimated spectrum as compared to existing calibration methods.

1. Introduction

From diagnosing diseases to inspecting critical industrial components, X-ray Computed Tomography (CT) has revolutionized how we explore the unseen. By combining X-rays or gamma rays with sophisticated mathematical algorithms, CT enables non-destructive three-dimensional visualization of internal structures with remarkable precision [1]. Its applications in medical imaging [2, 3], airport security checks [4–6], and industrial inspections [7, 8] have made it a cornerstone of modern technology.

Typical X-ray CT reconstructs an object's attenuation cross-section from transmission measurements acquired at multiple angles under the assumption of a monochromatic X-ray source [9]. This process has fundamental limitations, specifically with regard to quantitative characterization. First, the X-ray source emits a spectrum of energies rather than a single value, and its exact distribution is often unknown [10]. Second, the detector response varies with energy, meaning it does not record all photons equally [11, 12]. Third, material attenuation is inherently energy-dependent, causing different interactions across the spectrum [13]. Traditional CT reconstruction methods typically approximate the system as mono-energetic using average energy, neglecting the above factors, which can lead to inaccurate or suboptimal reconstructions [14].

More precisely, we use the term effective spectrum to denote the energy-dependent intensity recorded by the detector in a given system configuration with no object present. This intensity is not measured directly since typical detectors are energy-integrating, so each measurement aggregates multiple energies [15]. Although energy-resolving detectors exist, merely measuring the source spectrum remains challenging due to the unknown detector response [16]. Additionally, this effective system spectrum is affected by the characteristics of the X-ray source, any filters in use, and the detector (or scintillator).

Many CT applications can benefit from more accurate knowledge of the effective spectrum. For instance, beam hardening correction methods depend on an accurate spectral model to

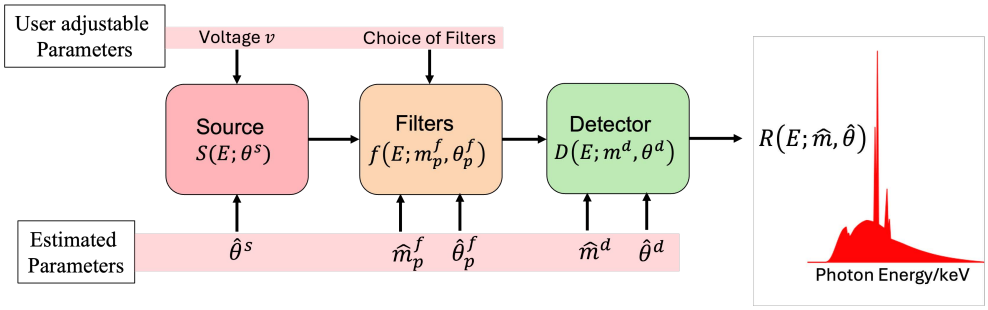

Fig. 1. **Effective Spectrum Model for an X-ray System.** The effective spectrum, $R(E)$, results from the combined effect of the source X-ray spectrum, the filters' responses, and the detector response. Each component is characterized by two sets of parameters: the user-adjustable parameters, such as source voltage and filter choice, which define the system configuration, and the estimated discrete and continuous parameters, which are unknown and inferred through the calibration process. Finally, we can calculate the effective spectrum with this model together with knowledge of the estimated parameters and the user-adjustable parameters.

mitigate nonlinear attenuation effects and improve image fidelity [14, 17]. Similarly, dual- and multi-energy CT techniques rely on precise spectral information to distinguish materials with similar attenuation properties, improving the estimation of atomic number and electron density [18]. Without proper characterization of the effective spectrum of the X-ray system, existing quantitative reconstruction methods [18–21] can suffer systematic errors, reducing the reliability of material classification and quantitative reconstructions. Especially, phase retrieval methods can potentially provide quantitative reconstruction with an accurate and effective spectrum [22, 23].

Accurately modeling the effective spectrum in poly-energetic CT systems is difficult since it is typically unknown and cannot be easily measured. One approach to accurately modeling the effective spectrum is to use physics simulations such as MCNP [24] or Geant4 [25]. However, the difficulty in this approach is that simulations depend on unknown physical parameters, such as the scintillator thickness and filter material composition. These parameters are typically unknown to the CT user. In some cases, the parameters may simply be difficult to measure, but in other cases, parameter values may be proprietary information that is not distributed by commercial vendors. Additionally, CT systems age and degrade over time, altering their spectral characteristics and rendering simulations based on initial parameter values inaccurate. Moreover, even energy-resolving detectors cannot directly measure the effective spectrum since the measured spectrum includes the response of the energy-resolving detector itself.

These challenges motivate the need for methods that can estimate the effective spectrum directly from calibration measurements performed by a user. To solve this ill-conditioned inverse problem, Tominaga et al. proposed both an iterative gradient descent method [26] and a singular-value decomposition (SVD) approach [27] to estimate the spectral distribution of X-rays. However, since this is a highly ill-conditioned inverse problem, [18, 28, 29] have proposed the use of regularization that reconstructs a smooth and continuous X-ray spectrum. However, in practice, the effective spectrum may exhibit discontinuities due to the characteristic lines of target materials like tungsten and the K-edges of scintillator materials [30].

An alternative approach, which we will refer to as bin-wise spectral calibration (BWSC), is to discretize the effective spectrum into multiple energy bins, and then impose some type of regularization on this discrete vector to address ill-conditioning and numerical instability issues. For example, Ruth et al. [31] introduced an iterative least-squares method with multiple

regularizations to accommodate discontinuities in the effective spectrum. Waggener et al. [32] incorporated nominal intensities into specific energy bins to estimate spectra with characteristic lines using a perturbation method. Leinweber et al. [33] proposed a prior-translated singular value decomposition (PTSVD) approach, separating the spectrum into high and low frequency components.

Another approach is to use a low-dimensional basis for spectral estimation, which can provide numerical stability along with the flexibility to incorporate characteristic lines and K-edges. Sidky et al. [34] represented the spectrum as a linear combination of B-splines and found a solution using the expectation–maximization (EM) algorithm. Zhao et al. [35] estimated the spectrum as a linear combination of six spectra generated by a Monte Carlo particle model. Liu et al. [36] introduced compressed sensing for spectrum estimation. Li et al. [37] proposed a dictionary-based spectral estimation (DictSE) method to estimate the X-ray effective system spectrum, employing an l_0 norm and a simplex constraint to ensure non-negative coefficients.

While these methods can estimate the effective spectrum, they are restricted to a fixed set of instrument settings. For example, if the source voltage is altered, the previous calibration and effective spectrum estimate become invalid. In such cases, the entire calibration process must be repeated from scratch, including both the collection of new data and the reprocessing of the measurements. This limitation makes these methods time-consuming for real-world applications, where instrument settings frequently change.

In this paper, we propose XCal, a multi-energy model-based spectral calibration method for X-ray CT. The XCal method estimates the effective spectrum of an X-ray CT scanning system using a few scans of known homogeneous samples at different source voltages. The method then uses this data to estimate the model parameters such as the anode take-off angle (reflection source), target thickness (transmission source), filter material and thickness, and scintillation detector material and thickness. An important advantage of XCal is that these parameters remain valid for different settings of user-adjustable parameters, such as the source voltage or filter choice. Consequently, the system does not need to be recalibrated each time user-adjustable parameters are changed.

At the core of XCal is a differentiable forward model of the CT system implemented in PyTorch [38]. Each physical component (source, filter, detector) is represented using a physics-based function parameterized by a combination of discrete and continuous parameters. This modular design enables automatic differentiation and optimization routines to work with multi-energy data, while also allowing the reuse of component model parameters across different CT configurations.

In this research, we introduce the following:

- A joint maximum likelihood loss function based on parametric, physics-based models of the source, filters, and detector using multi-energy measurements;
- A differentiable forward model of the CT system implemented in PyTorch, enabling gradient-based optimization of system parameters;
- An efficient algorithm for minimizing the loss using a mixed discrete and continuous optimization strategy;
- An open-source Python software implementation available at XCal, https://github.com/cabouman/xcal, with documentation at https://xcal.readthedocs.io/en/latest/index.html.

We evaluate XCal on both simulated and experimental datasets, and demonstrate that it significantly improves the accuracy of the estimated effective spectrum relative to existing methods. Additionally, our results show that incorporating multi-energy datasets into the calibration process improves the accuracy of system parameter estimates by an order of magnitude, making XCal a robust solution for practical CT spectral calibrations.

2. Forward Model

Figure 1 illustrates our spectral calibration approach. In contrast to a typical CT reconstruction, our goal is to estimate the X-ray system parameters and effective spectrum rather than to reconstruct the object being scanned. Hence, we use known calibration objects, such as K different wires, each with a known diameter and each made from a specific known material (more details are provided in Sections 2.4 and 2.5). We also assume that J measurements of the calibration objects are taken with varying X-ray energy and filter settings. We demonstrate below that including this diversity of information greatly improves the robustness and accuracy of our estimates.

2.1. The CT System Model

The X-ray CT system is modeled as the composition of a sequence of components comprised of a poly-energetic X-ray source, multiple unknown filters, calibration objects, and an energy-integrating scintillator-based detector. Our goal is then to determine the effective X-ray spectrum by estimating the discrete and continuous parameters of each system component from the measurements.

We use the following notation to model the components of the CT system:

- $S_j(E;\theta^s)$ - The X-ray source spectrum as a function of the photon energy, E, the scan index $j = 0,\dots,J-1$, and the unknown continuous source parameter, θ^s.
- $f(E;m^f,\theta^f)$ - The X-ray filter fractional transmission as a function of the unknown discrete material type parameter, m^f, and the unknown continuous material thickness parameter, θ^f.
- $D(E;m^d,\theta^d)$ - The X-ray detector response as a function of the unknown discrete scintillator material parameter, m^d, and the unknown continuous scintillator thickness parameter, θ^d.

The aggregate discrete and continuous system model parameters can then be formed by concatenating the parameters from each system component and are given by

$$m = (m_0^f,\dots,m_{P-1}^f,m^d) \tag{1}$$

$$\theta = (\theta^s,\theta_0^f,\dots,\theta_{P-1}^f,\theta^d)\ . \tag{2}$$

Here, we assume the possibility of P X-ray filters, each with its own material and thickness. In addition, we index the source by the scan index $j \in \{0,\dots,J-1\}$ since known source parameters, such as the peak X-ray voltage, may vary for each scan. We provide more details about this point in Section 2.2.

Using these parameters, we model the effective X-ray spectrum as the source spectrum modulated by the filters and detector:

$$R_j(E;m,\theta) = S_j(E;\theta^s)\cdot\left(\prod_{p\in B_j} f(E;m_p^f,\theta_p^f)\right)\cdot D(E;m^d,\theta^d)\ . \tag{3}$$

We will further assume that the known calibration object consists of K possible materials. Let i index a single projection pixel through the object (i.e., a single sinogram entry), and let $k \in \{0,\dots,K-1\}$ index one of the K materials in the calibration objects being scanned. Then, we may define the following known quantities:

- $\mu_k(E)$ - The linear attenuation coefficient (LAC) of the k^{th} material at energy E.

- $L_{k,i,j}$ - The length of intersection of the i^{th} projection ray with the k^{th} material for scan j.

From these known quantities, let $I_{i,j}$ represent the measured intensity for projection i and scan j, and let $I_{a,j}$ represent the corresponding air scan measurement, where no object is present. Then, these measurements are modeled using Beer–Lambert's law [9] as:

$$I_{i,j} = \int_0^\infty R_j(E;m,\theta) \cdot \exp\left(-\sum_{k=0}^{K-1} \mu_k(E) L_{k,i,j}\right) dE \tag{4}$$

$$I_{a,j} = \int_0^\infty R_j(E;m,\theta)\, dE, \tag{5}$$

And our forward model for the preprocessed measurements $y_{i,j}$ has the form

$$\begin{aligned} y_{i,j} &= \frac{I_{i,j}}{I_{a,j}} \\ &= \frac{\int_0^\infty R_j(E;m,\theta) \cdot \exp\left\{-\sum_{k=0}^{K-1} \mu_k(E) L_{k,i,j}\right\} dE}{\int_0^\infty R_j(E;m,\theta) dE} \\ &= \int_0^\infty \bar{R}_j(E;m,\theta) \cdot \exp\left\{-\sum_{k=0}^{K-1} \mu_k(E) L_{k,i,j}\right\} dE + \eta_{i,j}\ . \end{aligned} \tag{6}$$

where $\eta_{i,j}$ is assumed to be additive independent noise and

$$\bar{R}_j(E;m,\theta) = \frac{R_j(E;m,\theta)}{I_{a,j}} \tag{7}$$

is the normalized effective spectrum.

We discretize the energy domain by subdividing it into N_e non-overlapping bins $[E_b, E_{b+1}]$. For each bin, we define the discretized effective spectrum as:

$$r_{j,b}(m,\theta) = \int_{E_b}^{E_{b+1}} \bar{R}_j(E;m,\theta)\, dE. \tag{8}$$

Making the approximation that each $\mu_k(E)$ is constant within a bin, we define the contribution coefficient from the b^{th} energy bin to projection i and scan j as:

$$A_{i,j,b} = \exp\left(-\sum_{k=0}^{K-1} \mu_k(E_b) L_{k,i,j}\right), \tag{9}$$

where $A_{i,j,b}$ captures the attenuation for the b^{th} energy bin.

Using this discretization, the scaled transmission measurement of Eq. (6) becomes:

$$y_{i,j} \approx \sum_{b=0}^{N_e-1} A_{i,j,b}\, r_{j,b}(m,\theta) + \eta_{i,j}, \tag{10}$$

where $r_{j,b}(m,\theta)$ is the effective spectrum of the j^{th} scan in the b^{th} energy bin, $\eta_{i,j}$ is additive noise, and N_e is the total number of energy bins.

For all measurements in scan j, we can then express the forward model in the simpler form,

$$Y_j = A_j \vec{R}_j(m,\theta) + \eta_j\ , \tag{11}$$

where Y_j, A_j, $\vec{R}_j(m,\theta)$, and η_j are defined below.

- $Y_j \in \mathbb{R}^{M_j}$: A vector of normalized transmission measurements, defined as $Y_j = [y_{0,j}, \ldots, y_{M_j-1,j}]$.
- $A_j \in \mathbb{R}^{M_j \times N_e}$: The forward matrix representing contributions from N_e energy bins.
- $\vec{R}_j(m, \theta) \in \mathbb{R}^{N_e}$: The unknown discretized effective spectrum vector to be estimated.
- $\eta_j \in \mathbb{R}^{M_j}$: Additive noise affecting the measurements.

This forward model provides a framework for estimating the system parameters (m, θ) through calibration.

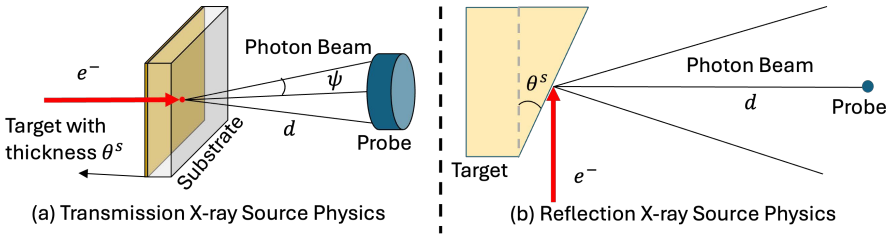

Fig. 2. **X-ray Source Physics.** Left: Transmission sources generate X-ray photons by passing high-energy electrons through a thin metallic anode target. Right: Reflection sources generate X-ray photons by directing high-energy electrons on a thick metallic anode with an angled surface.

Table 1: Source Lookup Table. We use existing software for each transmission and reflection case to simulate the source spectra for a discrete set of parameters and use linear interpolation for intermediate values.

Source Type:	Transmission	Reflection
Software:	Geant4	Spekpy
Estimated Parameters:	Target Thickness	Take-off Angle
User Adjustable Parameters:	Acceleration Voltage (kV)	
Other Parameters:	Target Material	
	Source-Detector Distance d (mm)	
	Energy Bin Width (keV)	
	Substrate*	
	Apex Angle θ^s (°)*	

* Applies only to Transmission setup.

2.2. Source Spectrum Model

In this section, we describe the model used for the source X-ray spectrum. There is no simple, analytical X-ray source model due to the diversity of X-ray tube designs and the complexity of their internal particle interactions. Consequently, we use existing X-ray modeling software to generate a precomputed lookup table at a discrete set of values of the unknown continuous parameters. Then, we use linear interpolation of the lookup table to define the source model for continuous parameter values.

Figure 2 illustrates the transmission and reflection X-ray sources parameters, and Table 1 details which parameters are estimated for each source type and which are assumed to be known.

We also note that the known user-adjustable parameters may vary for each scan and depend on the scan index j. The X-ray spectrum depends on a single unknown scalar, θ^s, for each source type. For transmission sources, θ^s represents the target thickness; for reflection sources, θ^s represents the take-off angle.

Using the fixed parameters and defining a physically realistic range for the estimated parameters, we generate a lookup table using either Geant4 [25] for the transmission source or SpekPy [39] for the reflection source. We first select discrete parameter values denoted by θ^s_q where $q \in \{0, \ldots, Q-1\}$. These discrete parameters are typically uniformly spaced over a physically realistic range of values. Then, for each discrete energy, E, we use the source modeling software to compute the lookup table entries given by

$$\mathcal{S}_{q,j}(E) = S_j(E; \theta^s_q) \; .$$

We use linear interpolation to evaluate $S_j(E; \theta^s)$ at values of θ^s not in the lookup table:

$$S_j(E; \theta^s) = (1-\gamma)\mathcal{S}_{q,j}(E) + \gamma \mathcal{S}_{q+1,j}(E) \; , \tag{12}$$

where $\gamma = \frac{\theta^s - \theta^s_q}{\theta^s_{q+1} - \theta^s_q}$ for $\theta^s_q \leq \theta^s < \theta^s_{q+1}$. The interpolation equation results in a continuous function that can be numerically differentiated everywhere except at the spline points. We note that PyTorch supports the gradient-based optimization of such functions since it is also used for the optimization of loss functions that use the commonly used ReLU function [40].

2.3. Filter and Detector Models

In this section, we describe the analytical models for the filter and detector functions. More specifically, for the filter, we use the following analytical model based on Beer–Lambert's law [41]

$$f\left(E; m^f_p, \theta^f_p\right) = \mathrm{e}^{-\mu(E; m^f_p)\theta^f_p} \; , \tag{13}$$

where $\mu(E; m^f_p)$ is the linear attenuation coefficient (LAC) for the material m^f_p at energy E.

For the detector response, we assume an energy-integrating detector based on scintillation. A scintillator in a detector converts the energy of absorbed X-ray photons into multiple visible-light photons [42]. Different scintillators have distinct K-edges, resulting in unique responses to incident X-ray photons. We represent the detector response as the product of the scintillator's X-ray photon absorption efficiency and the energy of the ionizing particle [43]. Then, based on the formula for X-ray photon absorption efficiency defined in equation (4) in [44], the scintillator response at energy E can be written as

$$D\left(E; m^d, \theta^d\right) = \frac{\mu^{en}(E; m^d)}{\mu(E; m^d)} \left(1 - \mathrm{e}^{-\mu(E; m^d)\theta^d}\right) E \; , \tag{14}$$

where m^d is the scintillator material, $\mu(E; m^d)$ is the LAC, $\mu^{en}(E; m^d)$ is the linear energy-absorption coefficient (LEAC) for this scintillator material, and θ^d is the scintillator thickness. The LAC $\mu(E; m^d)$ quantifies the fraction of photons removed from a beam per unit thickness of material due to both absorption and scattering processes. In contrast, the LEAC $\mu^{en}(E; m^d)$ measures the fraction of photon energy that is locally absorbed in the material, excluding energy lost to scattered photons [45]. Since scintillation arises from the energy deposited within the material rather than merely from photon attenuation, the above formula incorporates the ratio $\mu^{en}(E; m^d)/\mu(E; m^d)$ to account for the fraction of attenuated photons that deposit to the scintillator.

Algorithm 1 Computing Material Projection Lengths

Input: Physical samples made of K known materials
Output: Material projection lengths $L_{k,i,j}$

$s_j \leftarrow$ CTScanTarget() ▷ Measure the jth sinogram
$\hat{X}_j \leftarrow \text{FBP}(s_j)$ ▷ Reconstruct the volume
for $k = 0$ **to** $K - 1$ **do** ▷ Segment into K materials
    $\text{Mask}_{k,j} \leftarrow \text{Segment}(\hat{X}_j, \text{material } k)$
end for

▷ Forward project the binary mask
for $k = 0$ **to** $K - 1$ **do** ▷ for each material
    for $i = 0$ **to** $N - 1$ **do** ▷ for each projection
        $L_{k,i,j} \leftarrow \text{FP}_i(\text{Mask}_{k,j})$
    end for
end for

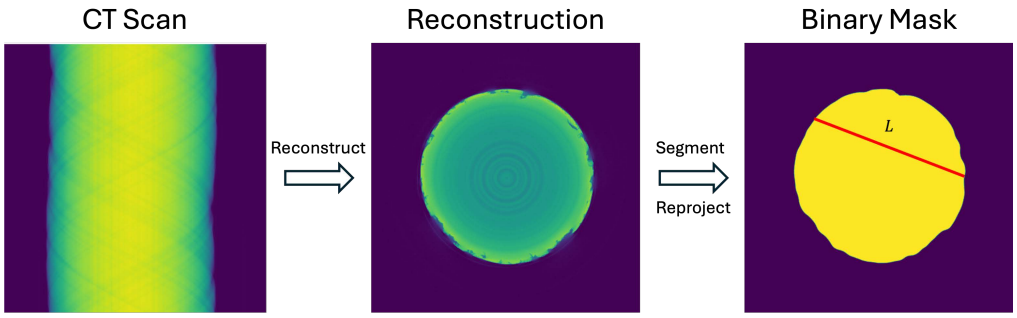

Fig. 3. **Computing Material Projection Lengths from a CT scan.** This example shows how to calculate projection lengths with a measured CT scan.

2.4. Model of Calibration Objects

The calibration objects are implicitly modeled through the values of the material projection lengths, $L_{k,i,j}$,. However, in practice, small variations in the calibration object's position and shape can adversely affect the calibration accuracy.

Figure 3 illustrates an example of how the projection lengths are accurately estimated from an initial full CT scan of the calibration objects. More specifically, for the j^{th} experiment we perform the following steps:

1. Scan the test object to obtain the sinogram s_j.
2. Reconstruct $\hat{X}_j$ from the sinogram s_j to form a 3D volumetric representation of the target object.
3. Segment the reconstructed volume into K distinct materials based on the object's known structure.
4. Perform a forward projection of each segmented material volume to obtain the material projection lengths $L_{k,i,j}$.

Algorithm 1 provides a pseudo-code specification of our method. Note that segmentation can be performed accurately without knowledge of the effective spectrum since we know the shape and material composition of the test object. In this case, we know the test object is a cylindrical

Algorithm 2 XCal Parameter Estimation Algorithm

Input: Set of possible filter and scintillator materials and range of possible values for the unknown continuous parameter

Output: Estimated material combination, $\hat{m}$, and parameter value, $\hat{\theta}$

▷ Get all combinations of filter and scintillator materials
$\mathcal{M} \leftarrow \mathcal{M}_0^f \times \ldots \times \mathcal{M}_{P-1}^f \times \mathcal{M}^d$
$\Theta \leftarrow \Theta^s \times \Theta_0^f \times \ldots \times \Theta_{P-1}^f \times \Theta^d$
$\mathcal{L} \leftarrow \{\}$ ▷ Mapping from material combinations to loss values
$C \leftarrow \{\}$ ▷ Mapping from material combinations to optimized continuous parameters
for $m \in \mathcal{M}$ **do** ▷ Search over all material combinations
    Initialize $\theta \leftarrow \frac{\theta_{\min}+\theta_{\max}}{2}$
    $\text{Loss}(m,\theta) \leftarrow \sum_j \frac{1}{2}\|Y_j - A_j\vec{R}_j(m,\theta)\|^2_{\Lambda_j}$
    $\hat{\theta} \leftarrow \arg\min_{\theta\in\Theta} \text{Loss}(m,\theta)$ ▷ Adam optimizer
    $\mathcal{L}[m] \leftarrow \text{Loss}(m,\hat{\theta})$ ▷ Save current results
    $C[m] \leftarrow \hat{\theta}$
end for
$\hat{m} \leftarrow \arg\min_m \mathcal{L}[m]$ ▷ Save optimal results
$\hat{\theta} \leftarrow C[\hat{m}]$

wire made of a homogeneous material. So we first form a standard reconstruction from the uncalibrated data. Next we apply Canny edge detection to extract the wire's boundary. Then we use binary filling to generate the segmentation mask.

2.5. Model of LAC and LEAC Material Properties

The models described above rely on estimates of the LAC, μ, and the LEAC, μ^{en}, for various materials. The NIST database provides tabulated values of the mass attenuation density, μ/ρ, and the mass energy-absorption coefficient, μ^{en}/ρ, for elemental materials where ρ is the density of the material in units of g/cm^3.

For compounds, $\mu(E)/\rho$ and $\mu^{en}(E)/\rho$ are determined as a weighted sum of the individual elements given by

$$\frac{\mu(E)}{\rho} = \sum_i w_i \cdot \left(\frac{\mu_i(E)}{\rho}\right) \tag{15}$$

where the weight w_i represents the fraction of the mass contribution of the specific element i to the total molecular mass. Once these quantities are computed, the values of μ and μ^{en} can be computed using the material's density listed in Table 14.

The tabulated NIST data is given at specific photon energy values E_q that are distributed on a log scale, ranging from 10^{-3} MeV to 10^2 MeV. For intermediate photon energy values within the range $E \in [E_q, E_{q+1})$, we use linear interpolation, also on a log scale, to compute $\mu(E)/\rho$ as follows:

$$\log\left(\frac{\mu(E)}{\rho}\right) = (1-\alpha)\log\left(\frac{\mu(E_q)}{\rho}\right) + \alpha\log\left(\frac{\mu(E_{q+1})}{\rho}\right) \tag{16}$$

where the interpolation factor α is given by: $\alpha = \frac{\log E - \log E_q}{\log E_{q+1} - \log E_q}$ This approach ensures the continuity of the LAC across a wide range of photon energies using logarithmic scaling.

3. Parameter Estimation using Loss Minimization

XCal estimates both the discrete and continuous parameters by numerically minimizing the following loss function based on the forward model defined in (11),

$$\text{Loss}(m, \theta) = \sum_{j=0}^{J-1} \frac{1}{2} \|Y_j - A_j \vec{R}_j(m, \theta)\|^2_{\Lambda_j} , \tag{17}$$

where Λ_j is a diagonal matrix with weights $\Lambda_j = \text{diag}(1/y_{i,j})$. Here, we assume that the noise variance is inversely proportional to the measured signal in order to approximately account for photon counting noise [3]. The parameter estimates, $(\hat{m}, \hat{\theta})$, are then given by the solution to the optimization problem

$$(\hat{m}, \hat{\theta}) = \underset{m \in \mathcal{M}, \theta \in \Theta}{\arg\min} \ \text{Loss}(m, \theta) , \tag{18}$$

where $\mathcal{M}$ represents the set of feasible discrete values of material choices for the filter and scintillator, and Θ defines the continuous parameter space, which is a product of intervals of continuous parameters.

We use the PyTorch software package [38] to solve the optimization of (18) for each fixed m. To do this, we implement the source, filter, and detector models as custom modules, allowing each component to be reused over multiple scans. The effective system spectrum, transmission function, and loss function are then implemented based on Eq. (3), (11), and (17). The parameters of each component are encapsulated to support repeated calls and allow optimization using built-in adjoint differentiation along with gradient descent optimization.

As detailed in Algorithm 2, the optimization algorithm is designed to solve the minimization problem of Eq. (18). The core strategy of the algorithm is to handle the discrete and continuous parameters separately. The outer loop of the algorithm performs an exhaustive search in the discrete parameter space $\mathcal{M}$, which includes various combinations of filters and scintillator materials. For each combination of these discrete parameters $m \in \mathcal{M}$, the algorithm initializes the continuous parameters $\theta \in \Theta$ using the center initialization, setting them at the midpoint of their respective bounds θ_{min} and θ_{max} and then performs a gradient-based search using the Adam optimizer [46], a gradient-based optimization approach using the constraints defined on line 3 of Algorithm 2.

The standard Adam optimizer does not inherently support enforcing constraints, so we enforce parameter bounds by implementing a custom clamping function. The custom clamping function uses the built-in torch.clamp function for the forward propagation and uses the identity for the back propagation. Intuitively, this models the derivative as 1 for all input values, even if they fall outside the clamped range. This results in the convergence of the Adam optimizer to a solution in the constraint set.

The optimal solution is selected based on the discrete parameter set $\hat{m}$ that yields the minimum total cost $\mathcal{L}[m]$. Finally, the continuous parameters $\hat{\theta}$ associated with this optimal discrete parameter set $\hat{m}$ are extracted, providing the complete set of optimal parameters $(\hat{m}, \hat{\theta})$ for the system.

4. Experimental Results

We compare our proposed XCal algorithm to existing methods on both simulated and measured datasets. In particular, we compare to the BWSC method implemented in Livermore Tomography Tools(LTT) [18] and the DictSE [37] method. We also compare to XCal-SingleE defined as XCal using only one scan at a single X-ray source voltage. This allows us to better understand the value of estimating model parameters using multi-energy data sets.

Finally, we used the center value of each parameter's range to initialize the XCal algorithm, and we used the same parameter values to calculate an initial effective spectrum for the BWSC method.

4.1. Data Pre-Processing

To enhance the accuracy of spectral estimation, we corrected the measurement data for various effects, including flux variation, gain effects, outliers, source blur, and detector blur. We corrected these effects before applying any spectral estimation algorithm to ensure the data were accurately represented, leading to more reliable calibration results.

Our measured datasets were acquired using two micro-CT systems: the Advanced Light Source (ALS) Beamline 8.3.2 and the Zeiss Xradia 510 Versa. Each dataset was pre-processed with the following steps, which ensure that the X-ray transmission through the air is normalized to 1, thereby allowing accurate transmission measurement for each sample within the system. *Step 1:* We normalized projection measurements using a reference air scan, which was obtained by averaging 15 scans without the object present. *Step 2:* We applied flux correction by first finding a "stamp region" of the normalized view in which unattenuated X-rays strike the detector. We then measure the average value in the stamp region and divide the entire normalized view by this value, so that the average value in the resulting stamp regions is 1, thus compensating for variations in background across views. *Step 3:* After flux correction, we applied a median filter with a 3x3 window to correct for outliers in the measurement data. The median filter is particularly effective for this purpose because it preserves edges while removing noise. *Step 4:* For only the Zeiss Versa 510 cone-beam X-ray data, we performed a deblurring operation using the SABER algorithm [47].

Table 2. Setup for simulated X-ray measurement scanning with different source voltages.

Dataset	**Low Voltage**	**Mid Voltage**	**High Voltage**
Scanned material	1 mm diam rods: V, Ti, Al, and Mg		
Source	Reflection X-ray source		
Voltage	50 kV	100 kV	150 kV
Take-off Angle*	[5,45] deg		
Tube Current	1 mAs		
Filter Material*	Randomly selected from filters in Table 14		
Filter Thickness*	Al: (0, 10] mm Cu: (0, 1] mm		
Scintillator Material*	Randomly selected from detectors in Table 14		
Scintillator Thickness*	[1, 500] μm		
Projection Geometry	Parallel beam		
Views	15 equally spaced		
Angle span	$\left[-\frac{\pi}{2}, \frac{\pi}{2}\right]$		
Detector Pixels	1024		
Pixel size	0.005 mm		

* Parameters to be estimated.

4.2. *Simulated Dataset Experiments*

In this section, we compare spectral calibration methods using 100 simulated datasets. Table 2 indicates that each simulated dataset used the same filter across three different voltages, and all datasets were generated using four distinct materials. Each dataset was generated using the X-rays as defined by Eq. (3) at three different voltages, with randomly generated model parameters having a uniform distribution over either their discrete values or their specified continuous values. Notice that aluminum and copper have very different attenuation properties; therefore, distinct thickness ranges are used for these two types of filters in our simulations. We generated Poisson noise for both the air and object scans individually, and our reflection source model used a lookup table with 11 evenly spaced values of the take-off angle in the range of 5 to 45 deg.

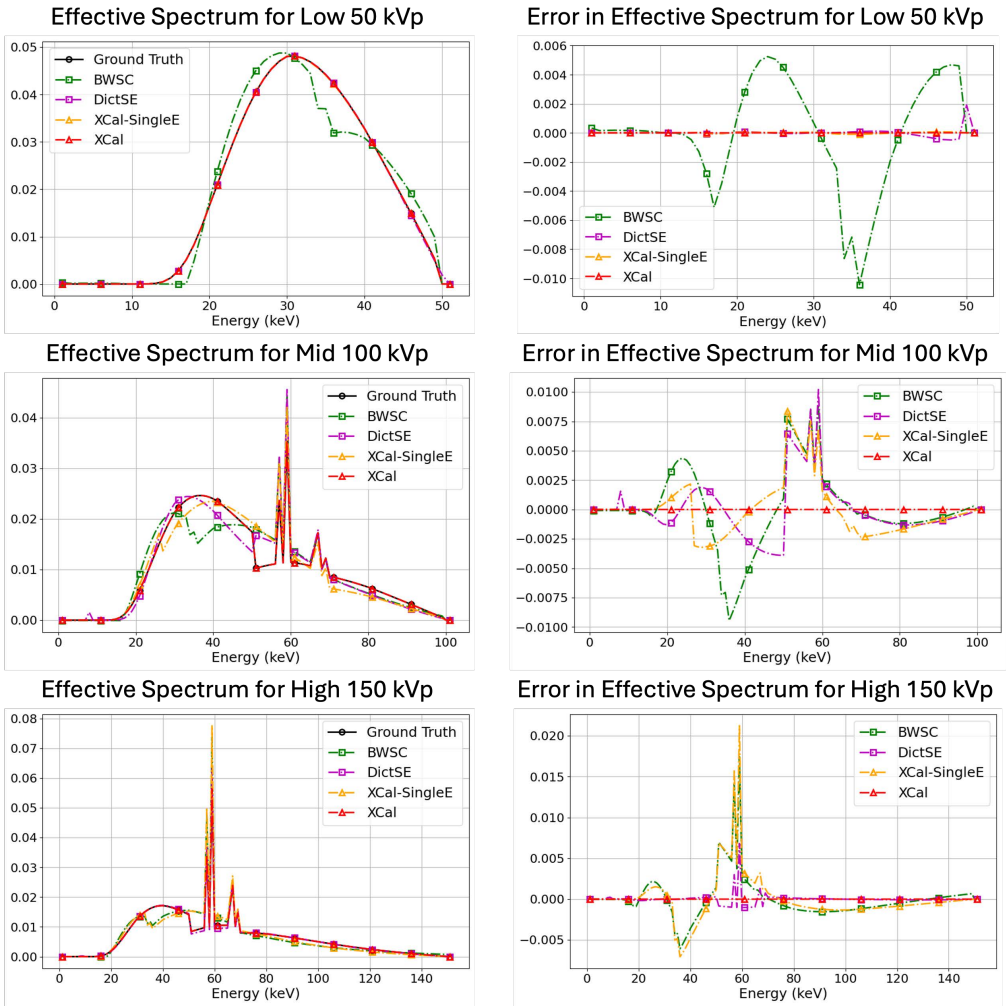

Fig. 4. **Simulated Dataset: Compare Estimated X-ray Effective Spectra with Ground-Truth.** Comparison of estimated effective spectra using different methods across three scans with varying source voltages: 50.0 kV (Top), 100.0 kV (Middle), and 150.0 kV (Bottom). The left column shows the estimated effective spectra, while the right column presents the difference between the estimated spectra and the ground truth. Notice that the XCal method has much lower error.

Figure 4 compares the estimated effective spectra and the ground truth for a single typical simulated dataset out of 100. Notice that the XCal method accurately estimates the effective spectrum for all three tested voltages of 50.0 kV, 100.0 kV, and 150.0 kV. In contrast, the BWSC method shows more significant deviations from the ground truth, especially at higher voltages. While the DictSE and XCal-SingleE methods show improved performance over BWSC, their spectral responses still fail to accurately capture the structure around the K-edge, highlighting the advantage of the full multi-energy calibration in XCal. The poorer performance of XCal-SingleE compared to XCal is likely due to the less well-conditioned nature of the inverse problem when using a single energy measurement.

Table 3 lists the NRMSE between the ground-truth and estimated normalized effective spectrum, $\bar{R}$, of (7) for each of the three tested voltages. Notice that the XCal method has the lowest error by a large margin in each case. In contrast, the BWSC method exhibited the highest average NRMSE values. The DictSE and XCal-SingleE methods performed better than BWSC but still had far higher errors than the XCal method.

Table 3. Average NRMSE between ground-truth and estimated normalized effective spectra for low-kV, mid-kV, and high-kV scans among 100 simulated datasets.

Scan \ Method	BWSC	DictSE	XCal-SingleE	XCal
Low-kV	0.0324	0.00552	0.00401	**0.00168**
Mid-kV	0.0219	0.00776	0.00509	**0.00103**
High-kV	0.0165	0.00753	0.00538	**0.00083**

* XCal jointly estimates all discrete and continuous parameters with all scans.

Tables 4 and 5 list metrics for the accuracy of the parameter estimation using both XCal and XCal-SingleE. Table 4 lists the success rate of estimating the correct discrete material for the 100 test examples. Notice that the XCal method achieves the highest accuracy for both the filter and scintillator materials, with greater than 93% accuracy. Table 5 lists the NRMSE of the estimated parameters. Again, the XCal method estimates the model parameters much more accurately than the SingleE method. This is again consistent with the conjecture that the MultiE inverse problem is much better conditioned than the SingleE inverse.

The results demonstrate that the XCal algorithm consistently achieves a higher success rate in estimating discrete parameters and lower NRMSE values for continuous parameters than XCal-SingleE. Furthermore, the results indicate that leveraging multi-energy datasets enhances parameter estimation accuracy, making XCal a more effective approach for model estimation.

Table 4: Success Rate of Estimated Discrete Parameters over 100 simulated datasets.

Parameters	Number of Options	XCal-SingleE Low-kV	XCal-SingleE Mid-kV	XCal-SingleE High-kV	XCal Combined
Filter material m_0^f	2	81%	83%	74%	**93%**
Scintillator material m^d	7	37%	58%	55%	**94%**

Table 5: Average NRMSE of Continuous Parameters over 100 simulated datasets

Parameters	Range	XCal-SingleE Low-kV	XCal-SingleE Mid-kV	XCal-SingleE High-kV	XCal Combined
Take-off angle θ^s (°)	[5, 45]	0.242	0.242	0.214	**0.044**
Filter thickness θ_0^f (mm)	[0, 10]	0.141	0.128	0.176	**0.054**
Scintillator thickness θ^d (μm)	[1, 500]	0.220	0.218	0.241	**0.070**

Table 6. Setup for the ALS X-ray measurement dataset.

Dataset	Low-filtration	High-filtration
Scanned material	1 mm diam rods: V, Ti, Al, and Mg	
Source	100 kV ALS Beamline 8.3.2 Synchrotron Light Source	
Filter 0's Material	Silicon	
Filter 0's Thickness*	(0,5] mm	
Filter 1's Material*	–	Aluminum
Filter 1's Thickness*	–	(0,10] mm
Scintillator Material*	Lu3Al5O12	
Scintillator Thickness*	[10,500] μm	
Projection Geometry	Parallel beam	
Views	2625	
Angle span	$[-\pi, \pi]$	
Detector Pixels	2048×2048	
Pixel size	$0.65\ \mu m \times 0.65\ \mu m$	
Blank scan photons/pixel	≈ 45000	≈ 500

* Parameters to be estimated.
– Filter not used.

4.3. Measured ALS Dataset Experiments

In this section, we compare spectral calibration methods using data measured at the Advanced Light Source (ALS) Beamline 8.3.2. This data includes a total of eight scans. Each scan has one homogeneous, 1mm diameter rod composed of one of V, Ti, Mg, and Al, each rod is scanned with two different filters. One filter has silicon only (low-filtration dataset), and one has silicon and aluminum (high-filtration dataset), as seen along with other parameters in Table 6. Since the objects are homogeneous, we run the spectral calibration algorithm using only 16 views and the center five slices in each scan. However, the full set of views is used to estimate the shape of each sample rod, as described in Section 2.4.

Since a ground-truth spectrum is not available for measured data, we use a leave-one-material-out cross-validation approach to evaluate our spectral calibration method. Since the effective spectrum should not depend on the selection of samples, we can measure the robustness of the

calibration method by measuring the standard deviation of estimated effective spectra varying for different excluded materials. Since we do have ground truth for material types (although not thicknesses), we can also get a rough measure of accuracy by determining the success rate in identifying the filter and scintillator materials.

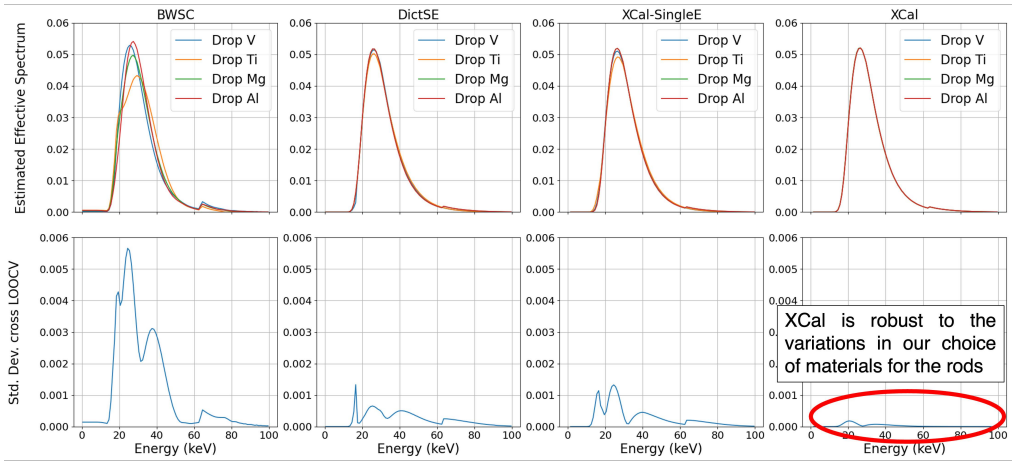

(a) Low-filtration.

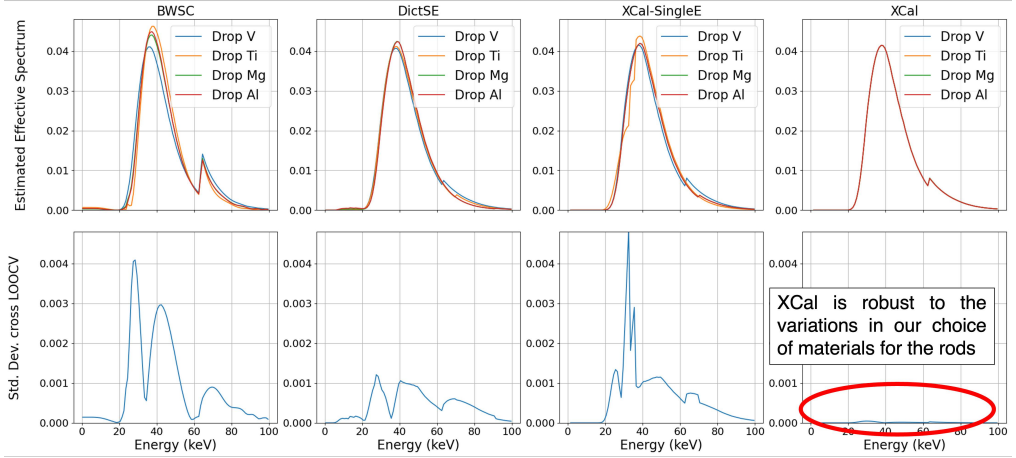

(b) High-filtration.

Fig. 5. **Comparison of estimated effective spectra using leave-one-material-out cross-validation on the ALS dataset.** (a) Low-filtration and (b) High-filtration. First row: estimated spectra; Second row: standard deviation across cross-validation cases. Column correspond to BWSC, DictSE, XCal-SingleE, and XCal. Notice that XCal is the most accurate.

Figure 5 compares the estimated effective spectrum from various approaches using leave-one-material-out cross-validation on the ALS dataset. Each column corresponds to a distinct method: BWSC, DictSE, XCal-SingleE, and XCal. The first row displays the estimated spectra in each figure, while the second row represents the standard deviation across cross-validation cases. Different colors indicate the exclusion of a specific material (V, Ti, Mg, Al) in the estimation process. It is evident from Figure 5 that XCal obtains the most consistent effective spectra estimate across all cross-validation cases (i.e., different material exclusions).

Table 7 presents the cross-validated NRMSE between the measured and predicted transmission

Table 7. Average Cross-Validation NRMS Deviation of Transmission Values

BWSC	DictSE	XCal-SingleE	XCal
0.0441	0.0313	0.0323	**0.0303**

values in the tomograhic views. So this measures how accurately the model predicts the actual measurements for the excluded material. We note that this is somewhat different than the error in the predicted effective spectrum itself. Again, the XCal method has the lowest error among the tested methods.

Table 8 reports the success rates of the discrete parameters estimated in four cross-validation cases of leave-one-material-out. The material of filter 1 is accurately estimated for all approaches based on the known ground truth-material choices. However, the scintillator material is accurately estimated only by the XCal method, which in this case achieves 100% accuracy.

Table 9 lists metrics associated with the accuracy of estimates for the continuous parameters in XCal. Notice that the XCal method results in estimated values of the parameter that are close to the nominal values indicated above each mean. Moreover, the XCal method also results in much lower standard deviation about the estimated value when different materials are excluded. This indicates that the XCal estimate is more robust than the other methods.

Table 8. Success rate of Estimated Discrete Parameters across 4 Leave-One-Out Cross-Validation Cases for the ALS X-ray Measurement Dataset.

Parameters	Number of Options	XCal-SingleE Low-filtration	XCal-SingleE High-filtration	XCal Combined
Filter 1 material, m_1^f	2	/	**100%**	**100%**
Scintillator material, m^d	7	50%	0%	**100%**

4.4. Measured Xradia 510 Versa Datasets

In this section, we compare methods using a dataset scanned with a Zeiss Xradia 510 Versa X-ray imaging system. The ZEISS Xradia 510 Versa is a widely used, high-resolution 3D X-ray imaging system for non-destructive analysis. This commercial micro-CT system uses a transmission X-ray source and operates with an adjustable source voltage ranging from 30 kV to 160 kV and produces bremsstrahlung X-ray spectra.

We collected multiple scans at different source voltages to obtain a multi-voltage dataset. Throughout this paper, we refer to these datasets as the Versa dataset. We used three different source voltages, capturing datasets at various energy levels, resulting in a multi-voltage dataset for three scanned samples.

Table 10 summarizes the scanning configuration used to acquire the multi-voltage dataset. It includes details about what was scanned and how the data was collected. In addition, the table provides all the necessary information to set up our optimization framework, which involves both discrete and continuous parameters.

Several key points should be noted: First, Eq. (12) defines an interpolated source spectrum model that requires a lookup table containing simulated transmission spectra for various target thicknesses. Second, while the scintillator material is known from the vendor, we also estimate it from a predefined list of possible detector materials (Table 14). This is motivated by the fact that obtaining the exact scintillator information experimentally is often difficult and time-consuming.

Table 9. Mean and Standard Deviation of Estimated Continuous Parameters over 4 Leave-One-Out Cross-Validation Cases for the ALS Dual-Energy X-ray Measurement Dataset. The XCal estimator exhibits a significantly lower standard deviation than XCal-SingleE, with values reduced by an order of magnitude, indicating much greater robustness.

Metric	**XCal-SingleE Low-filtration**	**XCal-SingleE High-filtration**	**XCal Combined**
	Filter 0 thickness, θ_0^f (mm) [0, 5] with nominal value of 2.0		
Mean	2.308	2.032	2.557
Std.	0.3441	0.4540	**0.0109**
	Filter 1 thickness, θ_1^f (mm) [0, 10] with nominal value of 8.0		
Mean	/	9.045	9.494
Std.	/	0.9264	**0.0303**
	Scintillator thickness, θ^d (μm) [10, 500] with nominal value of 50.0		
Mean	85.740	33.179	50.565
Std.	74.7912	14.9645	**1.5171**

Third, we acquired a full set of high-kV CT measurements for each sample rod to reconstruct their shapes using the method described in Sec. 2.4. In contrast, only a limited number of views were collected for the low- and mid-kV datasets since high-kV scans are more efficient to acquire while still maintaining an acceptable noise level.

As with the ALS data set of Section 4.3, we use leave-one-material-out cross-validation to assess the accuracy and robustness of the calibration methods. In this case, datasets consist of scans of three rods of different materials.

Figure 6 compares estimated effective spectra using four different spectral estimation approaches. The comparison is performed using leave-one-material-out cross-validation on the Versa dataset. In each subfigure, the first row displays the estimated spectra, while the second row presents the standard deviation across the three cross-validation cases, assessing the robustness of each method. The columns correspond to the four different estimation approaches mentioned above. In each plot, the spectra are plotted for three scenarios in which one of the materials (Al, Mg, Ti) is dropped from the dataset during the estimation process. These scenarios are represented by lines in blue (Drop Al), orange (Drop Mg), and green (Drop Ti). From Figure 6, we can see that the variation in the estimated spectrum caused by dropping specific materials is much lower for the XCal algorithm.

Table 11 lists the cross-validated NRMSE in the fit of the measurement data caused by dropping each of the three materials. Once again, the XCal algorithm has the lowest cross-validated NRMSE on the Versa dataset. Since this NRMSE is calculated in the measurement domain rather than the reconstructed effective spectrum domain, the reduction in NRMSE is smaller. However, in practice, we have found that this reduction corresponds to a significant enhancement in effective spectrum estimation accuracy.

Table 12 reports the success rates of the discrete parameters estimated in four cross-validation cases of leave-one-material-out based on the known ground-truth material types. The scintillator material is accurately estimated with the XCal-SingeE method using a Low-kV dataset and the XCal method.

Table 13 lists metrics associated with the accuracy of estimates for the continuous parameters in XCal. Notice that the XCal method also results in a much lower standard deviation about

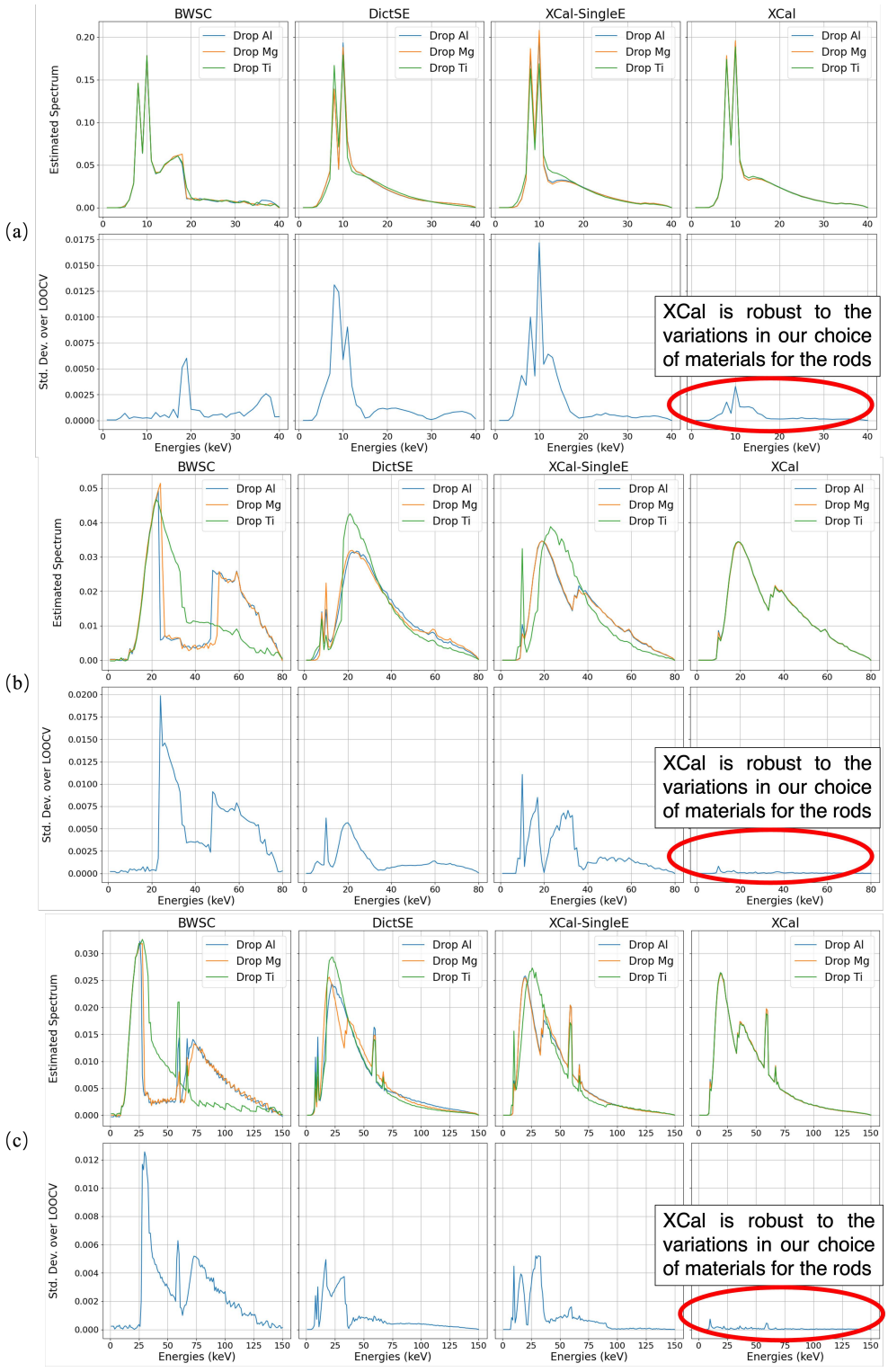

Fig. 6. **Comparison of estimated effective spectra using leave-one-material-out cross-validation on the Versa dataset.** (a) 40 kV, (b) 80 kV, and (c) 150 kV. First row: estimated spectra; Second row: standard deviation across cross-validation cases. Columns correspond to BWSC, DictSE, XCal-SingleE, and XCal. Notice that XCal is the most accurate.

Table 10. Setup for the Versa multi-voltage X-ray measurement dataset.

Dataset	**Low-kV**	**Mid-kV**	**High-kV**
Scanned material	1 mm diam rod: Ti, 0.5 mm diam rods: Al and Mg		
Source	Xradia 510 Versa Transmission X-ray Tube		
Voltage	40 kV	80 kV	150 kV
Target Thickness*	[1, 7] μm [48]		
Lookup Table	Simulated source spectra with target thickness at 1, 3, 5, and 7 μm		
Filter's Material	–	Aluminum	
Filter's Thickness*	–	[0, 10] mm	
Scintillator Material*	From Vendor		
Scintillator Thickness*	[1, 500] μm		
Projection Geometry	Cone-beam		
Source to Iso Distance	120 mm	120 mm	120 mm
Iso to Detector Distance	8 mm	8 mm	8 mm
Slit Collimator	✓		
Views	33	33	257
Angle span	$\left[-\frac{\pi}{2}, \frac{\pi}{2}\right]$	$\left[-\frac{\pi}{2}, \frac{\pi}{2}\right]$	$[-\pi, \pi]$
Detector Pixels	2048×2048		
Pixel size	$0.68\ \mu m \times 0.68\ \mu m$		
Blank Scan Photons/pixel	≈ 40000	≈ 21000	≈ 13000

* Parameters to be estimated.
– Filter not used.

Table 11. Average Cross-Validation NRMSE of Transmission Values for Versa Dataset

BWSC	**DictSE**	**XCal-SingleE**	**XCal**
0.0443	0.0415	0.0406	**0.0326**

the estimated value when materials are excluded. This indicates that the XCal estimate is more robust.

5. Conclusion

We propose XCal, a physics-based parametric model-based method to estimate the effective spectrum of an X-ray CT system. This model leverages multi-voltage or multi-filtration data, enabling more accurate and robust spectral estimation across different source voltages and filtration settings. XCal reduces the number of parameters by using a parametric representation of the CT system implemented with a differentiable forward model. This approach greatly reduces the ill-conditioning typically associated with spectral estimation, and it allows for easy reconfiguration of the model when user-defined system parameters, such as source voltage, are changed.

We applied the XCal algorithm to both simulated and measured datasets. The results demonstrate that XCal provides the highest accuracy and robustness in estimating the effective

Table 12. Success rate of Estimated Discrete Parameters for Versa Dataset.

Parameters	Number of Options	XCal-SingleE Low-kV	XCal-SingleE Mid-kV	XCal-SingleE High-kV	XCal Combined
Scintillator material, m^d	7	**100%**	66.7%	66.7%	**100%**

Table 13. Standard Deviation of Estimated Continuous Parameters for Versa Dataset.

Metric	XCal-SingleE Low-kV	XCal-SingleE Mid-kV	XCal-SingleE High-kV	XCal Combined
	Target thickness, θ^s (μm) [1, 7]			
Std.	1.247	2.103	1.460	**0.379**
	Filter 0 thickness, θ_0^f (mm) [0, 10]			
Std.	/	0.183	0.227	**0.019**
	Scintillator thickness, θ^d (μm) [1, 500]			
Std.	8.094	39.327	40.285	**1.822**

* Low-kV dataset does not use filter 0.

spectrum, even with changes in calibration materials. This is achieved through the accurate and robust estimation of system parameters, which is made possible by leveraging multi-energy datasets and a model-based, fully differentiable forward model of the X-ray CT system.

Although this study targets a single-source, multi-voltage or multi-filtration flat-panel setup, our differentiable framework is more flexible. Users can integrate customized differentiable PyTorch modules into the XCal package to support other advanced CT systems, such as dual-energy or multi-detector systems. These extensions, however, introduce additional parameters and require user to have a good understanding of their system.

With a broader trend toward differentiable computational imaging, our spectral calibration method, built on PyTorch, naturally aligns with modern frameworks like LEAP [49]. By leveraging auto-differentiation and GPU acceleration, our approach can be easily integrated into spectral CT reconstruction pipelines, enabling end-to-end optimization of both calibration and reconstruction. This may help inspire more sophisticated CT reconstruction algorithms in the future.

Appendix A:Interpolation of source spectrum over source voltage

Notice that the source voltage in an X-ray system can vary continuously and is not limited to a set of specific values; it is essential to have a model that works for any possible source voltage. To accurately handle any source voltage, we propose an interpolation function based on a list of source spectra and their corresponding voltages.

Let $v_0 < v_1$ be adjacent source voltages and let $S(E, v_0)$ and $S(E, v_1)$ be their associated effective system spectra. However, linear interpolation directly using $S(E, v_0)$ and $S(E, v_1)$ will not provide an accurate model because the X-ray system would not generate photons with an energy larger than the source voltage, which means $S(E, v_0)$ is zero for $E \geq v_0$. To resolve this, we extend $S(E, v_0)$ to $S'(E, v_0)$ by setting a negative value for $E > v_0$

$$S'(E, v_0) = \begin{cases} S(E), & E \leq v_0 \\ -\frac{E - v_0}{v_1 - v_0} S(E, v_1), & E > v_0 \end{cases} \tag{19}$$

where $r = \frac{E-v_0}{v_1-v_0}$.

Then, $S(E, v)$ for any $v_0 < v < v_1$ can be written as a bilinear interpolation between $S(E, v_0)$ and $S(E, v_1)$

$$S(E, v) = \frac{v_1 - v}{v_1 - v_0} S(E, v_0) + \frac{v - v_0}{v_1 - v_0} S(E, v_1) \tag{20}$$

The modification ensures that $S(E, v) = 0$ for any $E > v$.

Appendix B: Element and Compound Densities

Table 14. Element and Compound Densities for Filters and Detectors

Type	Material	Density ρ (g/cm^3)
Filter	Aluminum (Al)	2.70
	Copper (Cu)	8.92
Detector	CsI	4.51
	$Gd_3Al_2Ga_3O_{12}$	6.63
	$Lu_3Al_5O_{12}$	6.73
	$CdWO_4$	7.90
	$Y_3Al_5O_{12}$	4.56
	$Bi_4Ge_3O_{12}$	7.13
	Gd_2O_2S	7.32

Table 14 lists the material densities used in this paper. The possible scintillator materials for the detector are based on [50].

Funding. The U.S. Department of Energy by Lawrence Livermore National Laboratory under Contract DE-AC52-07NA27344 and LDRD project 22-ERD-011.

Acknowledgment. The information in this document is distributed under public release number LLNL-JRNL-871468. This work was performed under the auspices of the U.S. Department of Energy by Lawrence Livermore National Laboratory under Contract DE-AC52-07NA27344 and LDRD project 22-ERD-011. The authors acknowledge Dula Parkinson for his support during beamtime. Charles Bouman was partially supported by the Showalter Trust.

Disclosures. The authors declare no conflicts of interest.

Data Availability Statement. Data underlying the results presented in this paper are available in Ref. [51, 52]. Xradia 510 Versa Data are not publicly available at this time but may be obtained from the authors upon reasonable request.

References

1. P. J. Withers, C. Bouman, S. Carmignato, *et al.*, "X-ray computed tomography," Nat. Rev. Methods Primers **1**, 18 (2021).
2. B. Van Ginneken, B. Ter Haar Romeny, and M. Viergever, "Computer-aided diagnosis in chest radiography: A survey," IEEE Trans. on Med. Imaging **20**, 1228–1241 (2001).
3. J.-B. Thibault, K. D. Sauer, C. A. Bouman, and J. Hsieh, "A three-dimensional statistical approach to improved image quality for multislice helical CT," Med. physics **34**, 4526–4544 (2007).
4. S. Singh and M. Singh, "Explosives detection systems (eds) for aviation security," Signal Process. **83**, 31–55 (2003).
5. R. Anirudh, H. Kim, J. J. Thiagarajan, *et al.*, "Lose the views: Limited angle CT reconstruction via implicit sinogram completion," in *Proceedings of the IEEE Conference on Computer Vision and Pattern Recognition (CVPR),* (2018).
6. W. Li, G. T. Buzzard, and C. A. Bouman, "Sparse-view CT reconstruction using recurrent stacked back projection," in *2021 55th Asilomar Conference on Signals, Systems, and Computers,* (IEEE, 2021), pp. 862–866.
7. S. Carmignato, W. Dewulf, R. Leach *et al.*, *Industrial X-ray computed tomography*, vol. 10 (Springer, 2018).
8. L. De Chiffre, S. Carmignato, J.-P. Kruth, *et al.*, "Industrial applications of computed tomography," CIRP annals **63**, 655–677 (2014).
9. A. C. Kak and M. Slaney, *Principles of computerized tomographic imaging* (SIAM, 2001).

10. D. P. Clark and C. Badea, "Micro-CT of rodents: state-of-the-art and future perspectives," Phys. medica **30**, 619–634 (2014).
11. D. S. Maier, J. Schock, and F. Pfeiffer, "Dual-energy micro-CT with a dual-layer, dual-color, single-crystal scintillator," Opt. Express **25**, 6924–6935 (2017).
12. D. W. O'Connell, K. S. Morgan, G. Ruben, *et al.*, "Photon-counting, energy-resolving and super-resolution phase contrast X-ray imaging using an integrating detector." Opt. express **28**, 7080–7094 (2020).
13. A. Sarapata, M. Willner, M. Walter, *et al.*, "Quantitative imaging using high-energy X-ray phase-contrast CT with a 70 kVp polychromatic X-ray spectrum," Opt. express **23**, 523–535 (2015).
14. P. Jin, C. A. Bouman, and K. D. Sauer, "A model-based image reconstruction algorithm with simultaneous beam hardening correction for X-Ray CT," IEEE Trans. on Comput. Imaging **1**, 200–216 (2015).
15. T. Yanagida, "Inorganic scintillating materials and scintillation detectors," Proc. Jpn. Acad. Ser. B **94**, 75–97 (2018).
16. K. Taguchi, M. Zhang, E. C. Frey, *et al.*, "Modeling the performance of a photon counting x-ray detector for ct: energy response and pulse pileup effects," Med. physics **38**, 1089–1102 (2011).
17. R. A. Brooks and G. Di Chiro, "Beam hardening in X-ray reconstructive tomography," Phys. medicine & biology **21**, 390 (1976).
18. K. M. Champley, S. G. Azevedo, I. M. Seetho, *et al.*, "Method to extract system-independent material properties from dual-energy X-ray CT," IEEE Trans. on Nucl. Sci. **66**, 674–686 (2019).
19. M. Busi, K. A. Mohan, A. A. Dooraghi, *et al.*, "Method for system-independent material characterization from spectral X-ray CT," NDT & E Int. **107**, 102136 (2019).
20. S. G. Azevedo, H. E. Martz, M. B. Aufderheide, *et al.*, "System-independent characterization of materials using dual-energy computed tomography," IEEE Trans. on Nucl. Sci. **63**, 341–350 (2016).
21. D. Jumanazarov, J. Koo, M. Busi, *et al.*, "System-independent material classification through X-ray attenuation decomposition from spectral X-ray CT," NDT & E Int. **116**, 102336 (2020).
22. I. Häggmark, W. Vågberg, H. M. Hertz, and A. Burvall, "Comparison of quantitative multi-material phase-retrieval algorithms in propagation-based phase-contrast X-ray tomography," Opt. Express **25**, 33543–33558 (2017).
23. K. A. Mohan, J.-B. Forien, V. Sridhar, *et al.*, "Maximum likelihood based phase-retrieval using fresnel propagation forward models with optional constraints," IEEE Trans. on Comput. Imaging **9**, 1111–1125 (2023).
24. C. J. Werner, J. S. Bull, C. J. Solomon, *et al.*, "MCNP version 6.2 release notes," Tech. rep., Los Alamos National Laboratory (LANL), Los Alamos, NM (United States) (2018).
25. S. Agostinelli, J. Allison, K. a. Amako, *et al.*, "Geant4—a simulation toolkit," Nucl. instruments methods physics research section A: Accel. Spectrometers, Detect. Assoc. Equip. **506**, 250–303 (2003).
26. S. Tominaga, "The estimation of X-ray spectral distributions from attenuation data by means of iterative computation," Nucl. Instruments Methods Phys. Res. **192**, 415–421 (1982).
27. S. Tominaga, "A singular-value decomposition approach to X-ray spectral estimation from attenuation data," Nucl. Instruments Methods Phys. Res. Sect. A: Accel. Spectrometers, Detect. Assoc. Equip. **243**, 530–538 (1986).
28. C. H. Yan, R. T. Whalen, G. S. Beaupré, *et al.*, "Modeling of polychromatic attenuation using computed tomography reconstructed images," Med. Phys. **26**, 631–642 (1999).
29. B. Armbruster, R. J. Hamilton, and A. K. Kuehl, "Spectrum reconstruction from dose measurements as a linear inverse problem," Phys. Med. & Biol. **49**, 5087 (2004).
30. J. Hsieh, *Computed Tomography Principles, Design, Artifacts, and Recent Advances*, SPIE PM (Wiley, 2009).
31. C. Ruth and P. M. Joseph, "Estimation of a photon energy spectrum for a computed tomography scanner," Med. Phys. **24**, 695–702 (1997).
32. R. G. Waggener, M. M. Blough, J. A. Terry, *et al.*, "X-ray spectra estimation using attenuation measurements from 25 kVp to 18 MV," Med. physics **26**, 1269–1278 (1999).
33. C. Leinweber, J. Maier, and M. Kachelrieß, "X-ray spectrum estimation for accurate attenuation simulation," Med. physics **44**, 6183–6194 (2017).
34. E. Y. Sidky, Y. Lifeng, P. Xiaochuan, *et al.*, "A robust method of X-ray source spectrum estimation from transmission measurements: Demonstrated on computer simulated, scatter-free transmission data," J. Appl. Phys. **97** (2005).
35. W. Zhao, K. Niu, S. Schafer, and K. Royalty, "An indirect transmission measurement-based spectrum estimation method for computed tomography," Phys. Med. & Biol. **60**, 339 (2014).
36. L. Bin, Y. Hongrun, L. Huanwen, *et al.*, "A method of X-ray source spectrum estimation from transmission measurements based on compressed sensing," Nucl. Eng. Technol. **52**, 1495–1502 (2020).
37. W. Li, V. Sridhar, K. A. Mohan, *et al.*, "X-ray spectral estimation using dictionary learning," in *2023 IEEE International Conference on Image Processing (ICIP),* (2023), pp. 890–894.
38. A. Paszke, S. Gross, F. Massa, *et al.*, "Pytorch: An imperative style, high-performance deep learning library," in *Advances in Neural Information Processing Systems 32,* (Curran Associates, Inc., 2019), pp. 8024–8035.
39. G. Poludniowski, A. Omar, R. Bujila, and P. Andreo, "Spekpy v2. 0—a software toolkit for modeling X-ray tube spectra," Med. Phys. **48**, 3630–3637 (2021).
40. A. Jentzen and A. Riekert, "A proof of convergence for the gradient descent optimization method with random initializations in the training of neural networks with relu activation for piecewise linear target functions," J. Mach. Learn. Res. **23**, 1–50 (2022).
41. J. H. Lambert, *Photometria sive de mensura et gradibus luminis, colorum et umbrae* (Klett, 1760).
42. L. Lu, M. Sun, Q. Lu, *et al.*, "High energy X-ray radiation sensitive scintillating materials for medical imaging,

cancer diagnosis and therapy," Nano Energy **79**, 105437 (2021).
43. S.-G. Crystals, "Efficiency calculations for selected scintillators," Ohio, USA: Saint-Gobain (2014).
44. D. Cavouras, I. Kandarakis, S. Tsoukos, *et al.*, "A theoretical model for calculation of the detective quantum efficiency in granular scintillators," Appl. Radiat. Isot. **55**, 831–842 (2001).
45. A. Bos, "High sensitivity thermoluminescence dosimetry," Nucl. Instruments Methods Phys. Res. Sect. B: Beam Interactions with Mater. Atoms **184**, 3–28 (2001). Advanced Topics in Solid State Dosimetry.
46. D. P. Kingma and J. Ba, "Adam: A method for stochastic optimization," arXiv preprint arXiv:1412.6980 (2014).
47. K. A. Mohan, R. M. Panas, and J. A. Cuadra, "SABER: A systems approach to blur estimation and reduction in X-ray imaging," IEEE Trans. on Image Process. **29**, 7751–7764 (2020).
48. M. M. Nasseri, "Determination of tungsten target parameters for transmission X-ray tube: A simulation study using Geant4," Nucl. Eng. Technol. **48**, 795–798 (2016).
49. H. Kim and K. Champley, "Differentiable forward projector for x-ray computed tomography," arXiv preprint arXiv:2307.05801 (2023).
50. A. Yoneyama, R. Baba, and M. Kawamoto, "Quantitative analysis of the physical properties of CsI, GAGG, LuAG, CWO, YAG, BGO, and GOS scintillators using 10-, 20-and 34-keV monochromated synchrotron radiation," Opt. Mater. Express **11**, 398–411 (2021).
51. C. A. Bouman, "Xcal: X-ray Spectrum Calibration," https://github.com/cabouman/xcal (2025).
52. C. A. Bouman, "Xcal ALS Measurement Dataset," https://www.datadepot.rcac.purdue.edu/bouman/data/xcal_data.tgz (2025).